Dispersion and Stability Analysis for TLM Unstructured Block Meshing

Abdelrahman Ijjeh, Marylène Cueille, Jean-Lou Dubard, Michel Ney

Dispersion and Stability Analysis for TLM Unstructured Block Meshing

Abdelrahman A. Ijjeh, Marylène Cueille, *Member, IEEE*, Jean-Lou Dubard, *Member, IEEE*, and Michel M. Ney, *Life Fellow, IEEE*

***Abstract*— The insatiable demand to optimize and engineer new functionalities in electromagnetic devices has risen their geometrical complexity to unprecedented levels. This usually results in computationally multiscale problems with some tiny components of great importance to the overall behavior of these devices. Block meshing is a powerful technique for treating such problems. The usage of variable mesh size is adaptable for adequately representing the geometrical details without exhausting the computational resources with a uniform fine grid in the entire computational domain. In addition, block meshing allows the use of cubic cells only for which time step in maximum and velocity error is minimal in each subregion. In this article, we present a mathematical formulation for stability and dispersion analysis when using block meshing in the transmission-line matrix (TLM) method. These relations permit us to compute the maximum mesh size and time step that guarantee a tolerable level of numerical dispersion, hence minimizing the computational expenditures. Moreover, we study the case of adopting the local time step and demonstrate the origins of the instability that may appear in this case. Finally, some numerical experiments are presented to show the advantages of the proposed approach when using TLM block meshing. A similar procedure can be used for FDTD or FIT with block meshing.**

***Index Terms*— Block meshing, computational electromagnetics, global time step, local-time step, stability and dispersion analysis, time-domain methods, transmission-line matrix (TLM) method.**

I. Introduction

THE transmission-line matrix (TLM) method is a full-wave numerical scheme based on the analogy between Maxwell's equations and the voltages and currents propagating in a network of interconnected transmission lines [1], [2]. The symmetrical condensed node (SCN) developed in [2] is normally used in the TLM analysis because of its good dispersion characteristics and its ability to inherently operate at the maximum time step. The presence of media properties in the TLM-SCN node is taken into account either by a correction process at cells' centers for general complex linear media or by adding stubs for simple ones [2]–[7]. Therefore, no special treatment is required at the boundaries between different media for the SCN node. However, for other numerical schemes, such as the finite-difference time-domain (FDTD) method or the finite integration technique (FIT), an averaging process is necessary at the interface between different media [8]–[10]. Moreover, for typical frequency-domain techniques, such as Method of Moments (MoM) of the finite element method (FEM), the presence of complex material of heterogeneous anisotropic nature (such as anisotropic nonsaturated ferromagnetic objects) can be rather involved in terms of modeling the boundary conditions [11], [12].

The second main advantage of using the TLM technique comes from the inherited properties from the analogy with the circuit theory. Namely, for implementing subgridding (nonstructured meshing per block), one only needs an ideal transformer to model field exchange between coarse and fine regions in a perfect, lossless, and stable manner [13]–[15]. The meshing per block technique is very useful in minimizing the coarseness error that appears in multiscale problems by locally refining the mesh around fine details in the computational domain [14], [15]. Coarseness error occurs because, in such scenarios, the used mesh size is insufficient for accurately representing field spatial distribution in regions with fine details, such as corners and edges. This type of error can be significant even when using mesh size with negligible dispersion error ($dl \ll \lambda/10$) [15]. The multiscale nature can also originate if some subregions have physical properties that require much smaller cells, such as, for instance, the skin effect in lossy media at high frequencies [16]. It can also occur if the wavelength is much larger than the dimensions of the computational domain under consideration (for instance, the propagation of electromagnetic waves in the human brain in the range of 0.01–200 Hz) [17].

In the literature, one finds many proposed meshing per block algorithms in time-domain methods, such as in FDTD [18]–[22], FIT [23], the finite element time-domain (FETD) method [24], and TLM [13]–[15]. However, in the TLM method, the subgridding interface can cross heterogonous media, and it was successfully applied to complex materials, such as nonsaturated ferrite [15] or biological tissues [14]. One should keep in mind that, for FDTD and FIT, some empirical averaging should be done at the interface between different media. For instance, consider an example of subgridding with one large cell adjacent to N_s^2 small cells of different media properties among which some of them are dispersive and/or anisotropic. FDTD and FIT need an averag-

Abdelrahman A. Ijjeh, Marylène Cueille, and Jean-Lou Dubard are with the Laboratory of Electronic, Antennas and Telecommunications (LEAT), French National Research Council (CNRS), Université Côte d'Azur, 06903 Sophia Antipolis, France (e-mail: abdelrahman.ijjeh@univ-cotedazur.fr).

Michel M. Ney is with the Lab-STICC, IMT Atlantique, 29238 Brest, France (e-mail: michel.ney@imt-atlantique.fr).

ing algorithm at such an interface that requires additional operations. Moreover, that averaging induces some error. However, with TLM, the complexity of the media properties is taken into account at the cell centers. Therefore, the heterogeneity and the complexity of media do not have any impact on the subgridding TLM algorithm accuracy. Note that, in all previously mentioned techniques, the computational domain is supposed to operate at one global time step corresponding to the smallest Courant–Friedrichs–Lewy (CFL) time step limit [25]. Many attempts to use a local time step (namely, a time step that corresponds to the CFL limit in the block with a specific mesh size) have failed because of instability that often takes place after a few hundreds/thousands of iterations, depending on the application [14], [26].

Nevertheless, adoption of the local time step is very attractive [14]; it can substantially decrease the simulation CPU time and the numerical dispersion in cells for the following reasons: first, the number of cells with fine mesh size is normally much smaller than the total number of cells in practical simulations. Therefore, it avoids the waste of time when forcing large cells to follow the pace of smaller ones [14]. Second, the time step will correspond to the maximum CFL limit in every subdomain. Therefore, minimum numerical dispersion is guaranteed [2], [25].

Ijjeh and Ney [14] suggested an approach to overcome this instability when local time step is used, by low-pass filtering the time samples coming from fine meshes to the coarse ones. However, the proposed approach introduces a small attenuation at the interface between the two subdomains with different time steps [14]. It was found for many practical applications that the approach can be interesting because we can obtain useful simulation outputs before the signal is affected by this attenuation [14]. However, we do not find, in the literature, either a mathematical formulation that ensures the stability of the proposed approach or a mathematical demonstration that indicates the reason for this midterm to late time instability that occurs when no filtering is used. It is worth mentioning that an implicit technique was derived in [27] for FDTD subgridding. It is unconditionally stable and allows using a time step larger than the one dictated by the fine region. However, one should keep in mind that numerical dispersion in the ADI-FDTD [27] or SS-TLM [28] methods increases substantially when exceeding the CFL limit, especially for large subgridding ratios. This is why the authors are interested in finding a local time step-based algorithm, in which every subdomain uses its CFL limit.

The novelty of this article is twofold. First, it presents the TLM algorithm with block meshing in a concise matrix form in the spectral domain and states the necessary conditions for stability and the criteria for tolerable numerical dispersion error. Second, analytic expressions of matrices involved in stability analysis are fully derived to test block-meshing stability for local time step for a given N_s mesh ratio.

II. Mathematical Models of Dispersion in TLM

The numerical dispersion analysis generally stems from the study of plane waves propagating in an infinite mesh with homogeneous media properties [25], [29]–[34]. The outcome of this study is a mathematical relationship linking the frequency, mesh size, time step, constitutive parameters of the medium, and the direction of propagation [25], [29], [32]–[34]. The general procedure consists of modeling the eigenvalue problem that governs the temporal field updates and spatial propagation in the Hilbert space [25], [32]–[34].

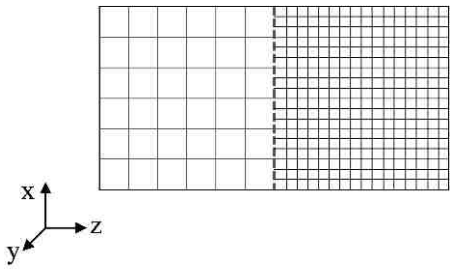

Fig. 1. Interface between two subdomains (dashed line); the interface is parallel to the xy plane, example with $N_s = 3$.

In the TLM method, there are several types of nodes that are generally used namely, symmetrical super condensed node (SSCN) [35], the hybrid SCN (HSCN) [36], and the previously mentioned SCN [2]–[5], [37]. However, in the following analysis, we will stick to the cubic SCN node because of its superior dispersion properties and its standard arm impedance (the free-space wave impedance η_o) regardless of the media properties [2], [35].

In this section, we will gradually build the general dispersion model for the unstructured Cartesian mesh. We start by revisiting the dispersion equations in the TLM method for the simple Cartesian uniform grid with the SCN nodes established previously [25], [33], [34]. The next step is to present the dispersion equations for the cells at the interface between two subdomains with different mesh sizes and global time steps. Finally, the dispersion relations at the interface between two subdomains with different mesh sizes and different local time steps will be presented.

To simplify the mathematical formulation and without loss of generality, we will assume that space is divided into two subspaces for the case of meshing per block, and the interface is parallel to the xy plane (as shown in Fig. 1). We will also assume that every cell in the left-hand subdomain is adjacent to an integer number N_s of smaller cells in the right-hand subdomain ($N_s = 3$ for instance in Fig.1).

A. Dispersion Equations for TLM in Cartesian Uniform Mesh

In this section, we recall the dispersion relationship in the case of uniform mesh with global time step given by [25]

$$\det(\overline{\overline{T}} - \overline{\overline{\Psi}}(\overline{\overline{\Lambda}}\,\overline{\overline{\Gamma}}(z)\overline{\overline{Q}} - \overline{\overline{\Phi}})) = 0 \tag{1}$$

where the matrix $\overline{\overline{T}}$ represents the time-shift operator (of elements $e^{j\omega\Delta T_{\mathrm{CFL}}}$), $\overline{\overline{\Psi}}$ represents the space-shift operator for the 18 voltages in the TLM-SCN node (connection matrix), $\overline{\overline{\Lambda}}$, $\overline{\overline{Q}}$, and $\overline{\overline{\Phi}}$ are rectangular matrices used by the TLM method to compute fields at node centers as in free space, and $\overline{\overline{\Gamma}}(z)$ represents the correction matrix that takes into account the

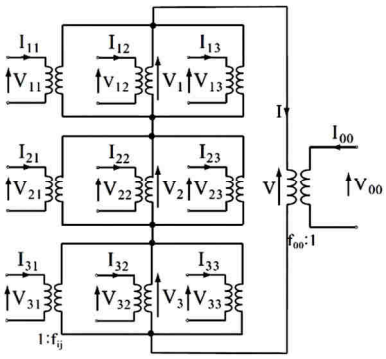

Fig. 2. Equivalent circuit schematic of the interface between the two domains (in Figs. 1 and 3) [13]–[15], [26].

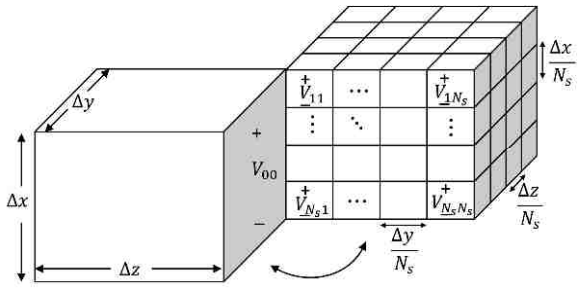

Fig. 3. Physical interface between two subdomains of different mesh size (see Fig. 1); one cell in left-hand subdomain is adjacent to N_s^2 cells in the right-hand one [14].

effect of media properties for a general linear medium. For more details regarding the previously mentioned matrices and their elements, we refer to [25], [37], and [38] for the reader.

The solution to the eigenproblem (1) gives the relationship between the media properties, the direction of propagation (vector $\vec{k}$), the frequency ω, the time step Δt, and the mesh size (Δx, Δy, Δz). Once this relationship is known, one can choose the appropriate mesh size for a tolerable level of numerical dispersion, and then, the maximum Δt that will guarantee stability can be computed [25].

B. Dispersion Equations for the Cells at the Interface Between Two Subdomains of Different Mesh Sizes and Global Time Steps

In the time domain, the interface between both subdomains (see Fig. 1) is modeled using the ideal transformer concept [13] (see Figs. 2 and 3). Voltage exchanges are governed by

$$v_{ij} = (I_i - I)\frac{Z_i}{f_{ij}} - u_{ij} \tag{2.a}$$

where

$$f_{ij} = \frac{\Delta x_{ij}}{\Delta y_{ij}} \tag{2.b}$$

$$f_{00} = -\frac{\Delta x_{00}}{\Delta y_{00}} \tag{2.c}$$

$$Z_i = \frac{1}{\sum_j Y_{ij}/f_{ij}^2} \tag{2.d}$$

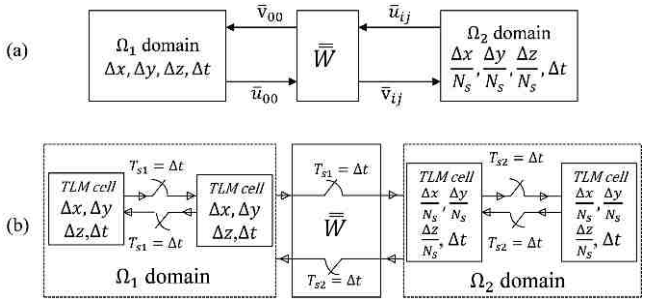

Fig. 4. (a) Block diagram of the interaction between the two subdomains Ω_1 and Ω_2. (b) Spatiotemporal interface with global time step (single-rate system); the interface transfer matrix $\overline{\overline{W}}$ is equivalent to (2.a).

$$I_i = 2\sum_j \frac{Y_{ij}u_{ij}}{f_{ij}} \tag{2.e}$$

$$I = \frac{\sum_i Z_i I_i}{\sum_i Z_i} \tag{2.f}$$

where voltages u_{ij} and v_{ij} are the incident and the reflected ones from the interface, respectively. Y_{ij} is the arm admittance that is always the reciprocal of the free-space characteristic impedance Z_o [2], [13]. The summations over i-index are for $i = \{0, 1, 2, \ldots, N_s\}$. The summations over j-index are for $j = \{1, 2, \ldots, N_s\}$ for $i > 0$ and consist of one element $j = 0$ when $i = 0$ [13]–[15].

Fig. 4 shows the block diagram of the voltage exchanges between the two subdomains of different mesh sizes. N_s is the subgridding ratio that is assumed to be an integer number.

As shown in Fig. 4, the operator $\overline{\overline{W}}$ is equivalent to (2.a) in the spectral domain. It governs the voltage exchanges between the subdomains Ω_1 and Ω_2 and vice versa. To derive the operator interface in the spectral domain, we start by rewriting (2.a) in a more explicit form

$$v_{ij} = -u_{ij} + \left(2\sum_k \frac{Y_{ik}u_{ik}}{f_{ik}} - \frac{\sum_l Z_l I_l}{\sum_l Z_l}\right)\frac{Z_i}{f_{ij}}. \tag{3}$$

For the case of TLM-SCN node with cubic cells, the arm admittances Y_{ij} are always that of the reciprocal of free-space impedance η_o and the aspect ratio $f_{ij} = 1 \forall i, j \in \{0, \ldots, N_s\}$. Z_i and I_i (2.d), (2.e) are simplified to

$$Z_i = \frac{1}{\sum_j Y_{ij}/f_{ij}^2} = \begin{cases} \eta_o, & i = 0 \\ \dfrac{\eta_o}{N_s}, & i > 0 \end{cases} \tag{4.a}$$

$$I_i = \frac{2}{\eta_o}\sum_j u_{ij} = \begin{cases} \dfrac{2}{\eta_o}u_{00}, & i = 0 \\ \dfrac{2}{\eta_o}\displaystyle\sum_{j=1}^{Ns} u_{ij}, & i > 0. \end{cases} \tag{4.b}$$

The current I in (2.f) can be written as

$$\begin{aligned} I &= \frac{\sum_i Z_i I_i}{\sum_i Z_i} \\ &= \frac{Z_0 I_0 + \sum_{\mathrm{i}=1}^{Ns} Z_i I_i}{Z_0 + \sum_{\mathrm{i}=1}^{Ns} Z_i} \\ &= \frac{1}{\eta_o}\left(u_{00} + \frac{1}{N_s}\sum_{\mathrm{j}=1}^{Ns}\sum_{i=1}^{Ns} u_{ij}\right). \end{aligned} \tag{4.c}$$

Then, the reflected voltages v_{pq} in (3) become

$$v_{pq} = \begin{cases} \dfrac{1}{N_s}\displaystyle\sum_{j=1}^{Ns}\sum_{i=1}^{Ns} u_{ij}, \quad p,q = 0 \\ -u_{pq} + \dfrac{1}{N_s}\left(2\displaystyle\sum_{j=1}^{Ns} u_{pj} - u_{00} - \dfrac{1}{N_s}\displaystyle\sum_{j=1}^{Ns}\sum_{i=1}^{Ns} u_{ij}\right) \\ \quad p,q \neq 0. \end{cases} \tag{5}$$

To make the formulation more concise, we define the matrices $\overline{\overline{u}}$ and $\overline{\overline{v}}$ of incident and reflected voltages, respectively, at the interface from the right-hand side of the interface (in the fine region)

$$\overline{\overline{u}} = \begin{bmatrix} u_{11} & \cdots & u_{1N_s} \\ \vdots & \ddots & \vdots \\ u_{N_s 1} & \cdots & u_{N_s N_s} \end{bmatrix} \tag{6.a}$$

$$\overline{\overline{v}} = \begin{bmatrix} v_{11} & \cdots & v_{1N_s} \\ \vdots & \ddots & \vdots \\ v_{N_s 1} & \cdots & v_{N_s N_s} \end{bmatrix}. \tag{6.b}$$

In the special case of reflection toward the coarse mesh corresponding to $p = 0$ and $q = 0$, (5) becomes

$$v_{00} = \frac{1}{N_s}\overline{e}\,\overline{\overline{u}}\,\overline{e}^T \tag{7.a}$$

where $\overline{e}^T$ is a column vector of length N_s whose entries are all ones. In the reflections toward the small cells corresponding to $p \neq 0$ and $q \neq 0$, (5) can be written in the matrix form as

$$\overline{\overline{v}} = -\overline{\overline{u}} + \frac{1}{N_s}\overline{\overline{O}}_{N_s}\left(2\overline{\overline{u}} - u_{00}\overline{\overline{I}}_{N_s} - \frac{1}{N_s}\overline{e}\,\overline{\overline{u}}\,\overline{e}^T\overline{\overline{I}}_{N_s}\right) \tag{7.b}$$

where $\overline{\overline{O}}_{N_s}$ is a square matrix of size N_s, with all its elements of unity, and $\overline{\overline{I}}_{N_s}$ is the identity matrix of rank N_s.

After some mathematical manipulations and substituting (7.a) into (7.b), it can be written as

$$\overline{\overline{v}} = \overline{\overline{H}}\,\overline{\overline{u}} - \frac{1}{N_s}\overline{\overline{I}}_{N_s}(u_{00} + v_{00}) \tag{8}$$

where the matrix $\overline{\overline{H}}$ is given by

$$\overline{\overline{H}} = 2\overline{\overline{O}}_{N_s}/N_s - \overline{\overline{I}}_{N_s}. \tag{9}$$

The incident /reflected voltages ($\tilde{u}_{pq}$ and $\tilde{v}_{pq}$) in the spectral domain [corresponding to v_{pq} and u_{pq} for indices $p,q \in \{1,\ldots,N_s\}$ in Figs. 3 and 4(a)] can be linked to corresponding values in their neighboring small cells by a space shift operator as

$$\tilde{u}_{pq} = e^{j2\pi(\Delta x k_x + \Delta y k_y)/Ns}\tilde{u}_{p-1,q-1} \tag{10.a}$$

$$\tilde{v}_{pq} = e^{j2\pi(\Delta x k_x + \Delta y k_y)/Ns}\tilde{v}_{p-1,q-1}. \tag{10.b}$$

Both (7.a) and (8) can be written in the spectral domain as

$$\tilde{v}_{00} = \frac{1}{N_s}\overline{e}\,\overline{\overline{S}}\,\overline{e}^T\tilde{u}_{11} \tag{11.a}$$

$$\tilde{\overline{\overline{v}}} = \overline{\overline{H}}\,\overline{\overline{S}}\tilde{u}_{11} - \frac{1}{N_s}\overline{\overline{I}}_{N_s}(\tilde{u}_{00} + \tilde{v}_{00}) \tag{11.b}$$

with $\overline{\overline{S}}$ matrix elements being

$$(\overline{\overline{S}})_{pq} = \zeta(p,q) \quad \forall p,q \in \{1,\ldots,N_s\} \tag{12.a}$$

$$\zeta(p,q) = e^{j2\pi(\Delta x(p-1)k_x + \Delta y(q-1)k_y)/Ns}. \tag{12.b}$$

The idea behind using this space shift operator is to represent the matrix $\tilde{\overline{\overline{v}}}$ or $\tilde{\overline{\overline{u}}}$ in (6.a) and (6.b), respectively, with one single element in these matrices $\tilde{v}_{11}$ or $\tilde{u}_{11}$ and a field-independent space shift operator $\overline{\overline{S}}$.

To obtain the dispersion relationship for cells adjacent to the interface, we start by the cells in Ω_1 at the left-hand side. Normally, the cell dispersion phenomenon is governed by (1) in the absence of this interface. Therefore, we can expect some modification to (1), especially for the voltages/fields that are coming from the right-hand side. The temporal shift operator is very similar except that we use a global time step and, hence, a fraction of the CFL time limit in large cells with $\Delta t = \Delta T_{\mathrm{CFL}}/N_s$; thus,

$$\overline{\overline{T}} = e^{j\omega\Delta t}\overline{\overline{I}}_{18} \tag{13.a}$$

$$\overline{V}_{\mathrm{inc}}^{\Omega_1,n+1} = \overline{\overline{T}}\,\overline{V}_{\mathrm{inc}}^{\Omega_1,n} \tag{13.b}$$

where $\overline{\overline{I}}_{18}$ is the identity matrix of rank 18 (equivalent to number of arms in the SCN node), $\overline{V}_{\mathrm{inc}}^{\Omega_1,n}$ is the array of the 18 incident voltages on the SCN arms at time step n (14.c), and ω is the angular frequency of the propagating wave.

The reflected voltages from a TLM-SCN cell are expressed as a linear combination of the incident voltages and the fields computed at the center of the cell [25], [37], which yields

$$\overline{V}_{\mathrm{ref}}^{\Omega_1,n} = \overline{\overline{\Lambda}}\,\overline{F}_n - \overline{\overline{\Phi}}\,\overline{V}_{\mathrm{inc}}^{\Omega_1,n} \tag{14.a}$$

$$\overline{V}_{\mathrm{ref}}^{\Omega_1,n} = \begin{bmatrix} V_{\mathrm{ref},1}^{\Omega_1} & V_{\mathrm{ref},2}^{\Omega_1} & \cdots & V_{\mathrm{ref},18}^{\Omega_1} \end{bmatrix}_n^T \tag{14.b}$$

$$\overline{V}_{\mathrm{inc}}^{\Omega_1,n} = \begin{bmatrix} V_{\mathrm{inc},1}^{\Omega_1} & V_{\mathrm{inc},2}^{\Omega_1} & \cdots & V_{\mathrm{inc},18}^{\Omega_1} \end{bmatrix}_n^T \tag{14.c}$$

$$\overline{F}^n = \begin{bmatrix} E_x & E_y & E_z & H_x & H_y & H_z \end{bmatrix}_n^T \tag{14.d}$$

where $\overline{V}_{\mathrm{ref}}^{\Omega_1,n}$ and $\overline{F}^n$ are the reflected voltages and the computed fields at the node center, respectively. T is the matrix transpose operator.

The electric and magnetic fields inside the SCN node are defined as a linear combination of the incident voltages [25]

$$\overline{F}^n = \overline{\overline{Q}}\,\overline{\overline{\Gamma}}(z)\overline{V}_{\mathrm{inc}}^{\Omega_1,n} \tag{15}$$

where the matrix $\overline{\overline{Q}}$ represents an operator that maps voltages that correspond to each field component, and $\overline{\overline{\Gamma}}(z)$ is the correction matrix that contains time-domain filters [25].

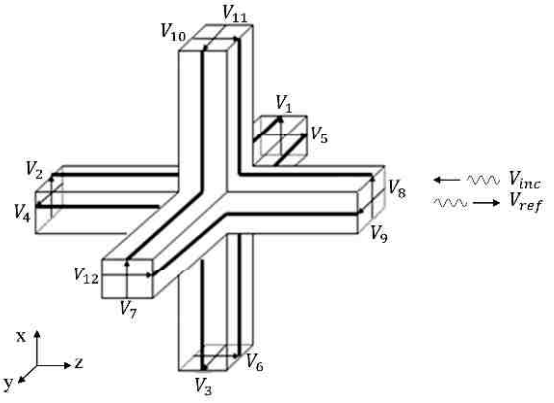

Fig. 5. TLM-SCN node, with six arms, 12 voltages for communicating with neighboring cells, and six internal voltages (used in noncubic cells, nonfree-space media, or when operating on Δt inferior to the CFL limit) [2], [31].

This matrix depends on constitutive parameters of the medium and governs the field–material interaction inside the TLM node [5], [25].

As shown in Fig. 5, incident voltages for the next time step are written in terms of reflected voltages from the neighboring cells at the current time step as

$$\begin{pmatrix} V_{\text{inc},1} \\ V_{\text{inc},2} \\ V_{\text{inc},3} \\ V_{\text{inc},4} \\ V_{\text{inc},5} \\ V_{\text{inc},6} \\ V_{\text{inc},7} \\ V_{\text{inc},8} \\ V_{\text{inc},9} \\ V_{\text{inc},10} \\ V_{\text{inc},11} \\ V_{\text{inc},12} \\ V_{\text{inc},13} \\ V_{\text{inc},14} \\ V_{\text{inc},15} \\ V_{\text{inc},16} \\ V_{\text{inc},17} \\ V_{\text{inc},18} \\ \end{pmatrix}_{n+1} = \begin{pmatrix} V_{\text{ref},12}(k,l-1,m) \\ V_{\text{ref},9}(k,l,m-1) \\ V_{\text{ref},11}(k-1,l,m) \\ V_{\text{ref},8}(k,l,m-1) \\ V_{\text{ref},7}(k,l-1,m) \\ V_{\text{ref},10}(k-1,l,m) \\ V_{\text{ref},5}(k,l+1,m) \\ V_{\text{ref},4}(k,l,m+1) \\ V_{\text{ref},2}(k,l,m+1) \\ V_{\text{ref},6}(k+1,l,m) \\ V_{\text{ref},3}(k+1,l,m) \\ V_{\text{ref},1}(k,l+1,m) \\ V_{\text{ref},13}(k,l,m) \\ V_{\text{ref},14}(k,l,m) \\ V_{\text{ref},15}(k,l,m) \\ V_{\text{ref},16}(k,l,m) \\ V_{\text{ref},17}(k,l,m) \\ V_{\text{ref},18}(k,l,m) \\ \end{pmatrix}_{n}. \tag{16}$$

Now, incident voltages can be represented in the Hilbert space [22], [29] as a function of reflected voltages

$$\overline{V}_{\text{inc}}^{\Omega_1,n+1} = \overline{\overline{\Psi}}_{\partial\Omega_1} \overline{V}_{\text{ref}}^{\Omega_1,n} \tag{17}$$

where $\overline{\overline{\Psi}}_{\partial\Omega_1}$ is a modified space shift operator (the connection matrix) that takes into account the effect of the interface

$$\overline{\overline{\Psi}}_{\partial\Omega_1} = \begin{pmatrix} 0 & \overline{\overline{\psi}}_1 & 0 \\ \overline{\overline{\psi}}_2 & 0 & 0 \\ 0 & 0 & \overline{\overline{I}}_6 \end{pmatrix} \tag{18}$$

TABLE I

SPACE-SHIFT OPERATORS IN THE SPECTRAL DOMAIN AND THE HILBERT SPACE FOR $\partial\Omega_1$ SUBDOMAIN (SEE FIG. 6)

Spectral domain notation	Hilbert stapce notation
$X^\dagger = e^{-j\chi}$	$X^\dagger \lvert n;k,l,m\rangle = \lvert n;k-1,l,m\rangle$
$X = e^{j\chi}$	$X \lvert n;k,l,m\rangle = \lvert n;k+1,l,m\rangle$
$Y^\dagger = e^{-j\eta}$	$Y^\dagger \lvert n;k,l,m\rangle = \lvert n;k,l-1,m\rangle$
$Y = e^{j\eta}$	$Y \lvert n;k,l,m\rangle = \lvert n;k,l+1,m\rangle$
$Z^\dagger = e^{-j\xi}$	$Z^\dagger \lvert n;k,l,m\rangle = \lvert n;k,l,m-1\rangle$
$Z = e^{\frac{j\xi}{2}(1+\frac{1}{N_s})}$	$Z \lvert n;k,l,m\rangle = \lvert n;k,l,m+1\rangle$

where $\overline{\overline{\psi}}_1$ and $\overline{\overline{\psi}}_2$ write

$$\overline{\overline{\psi}}_1 = \begin{pmatrix} 0 & 0 & 0 & 0 & 0 & Y^\dagger \\ 0 & 0 & Z^\dagger & 0 & 0 & 0 \\ 0 & 0 & 0 & 0 & X^\dagger & 0 \\ 0 & Z^\dagger & 0 & 0 & 0 & 0 \\ Y^\dagger & 0 & 0 & 0 & 0 & 0 \\ 0 & 0 & 0 & X^\dagger & 0 & 0 \end{pmatrix} \tag{19.a}$$

$$\overline{\overline{\psi}}_2 = \begin{pmatrix} 0 & 0 & 0 & 0 & Y & 0 \\ 0 & 0 & 0 & Z & 0 & 0 \\ 0 & Z & 0 & 0 & 0 & 0 \\ 0 & 0 & 0 & 0 & 0 & X \\ 0 & 0 & X & 0 & 0 & 0 \\ Y & 0 & 0 & 0 & 0 & 0 \end{pmatrix} \tag{19.b}$$

and elements of the above matrices are defined in Table I.

In the above χ, η, and ξ are the normalized spatial frequencies. In analogy with $\omega\Delta$t in (13.a), they are defined by [25], [32]–[34]

$$\chi = 2\pi\,\Delta x k_x \tag{20.a}$$

$$\eta = 2\pi\,\Delta y k_y \tag{20.b}$$

$$\xi = 2\pi\,\Delta z k_z. \tag{20.c}$$

Now comes the important step, where symmetry is broken, and the voltages in both Ω_1 and Ω_2 domains are coupled. Namely, $V_{\text{inc},9}$ and $V_{\text{inc},8}$ in Ω_1 depend on $V_{\text{ref},2}$ and $V_{\text{ref},4}$ coming from small cells in Ω_2 and vice versa. Based on (11.a), these voltages can be written as

$$V_{\text{inc},9}^{\Omega_1}(k,l,m) = \frac{1}{N_s}\overline{e}\,\overline{\overline{S}}\,\overline{e}^T \tilde{u}_{2,11} \tag{21.a}$$

$$V_{\text{inc},8}^{\Omega_1}(k,l,m) = \frac{1}{N_s}\overline{e}\,\overline{\overline{S}}\,\overline{e}^T \tilde{u}_{4,11}. \tag{21.b}$$

Following a similar procedure for cells in Ω_2 as in (11.b) yields

$$V_{\text{inc},2}^{\Omega_2}(p,q,m+1) = (\overline{\overline{H}}\,\overline{\overline{S}})_{pq}\tilde{u}_{2,11} - \frac{1}{N_s}\overline{\overline{I}}_{N_s}\left(V_{\text{ref},9}^{\Omega_1}(k,l,m) + \frac{1}{N_s}\overline{e}\,\overline{\overline{S}}\,\overline{e}^T\tilde{u}_{2,11}\right) \tag{22.a}$$

$$V_{\text{inc},4}^{\Omega_2}(p,q,m+1) = (\overline{\overline{H}}\,\overline{\overline{S}})_{pq}\tilde{u}_{4,11} - \frac{1}{N_s}\overline{\overline{I}}_{N_s}\left(V_{\text{ref},8}^{\Omega_1}(k,l,m) + \frac{1}{N_s}\overline{e}\,\overline{\overline{S}}\,\overline{e}^T\tilde{u}_{4,11}\right) \tag{22.b}$$

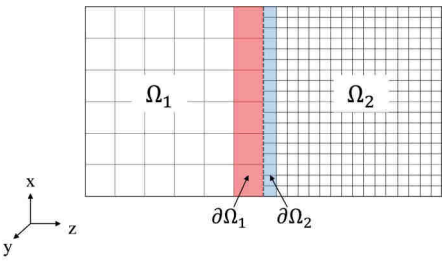

Fig. 6. Four regions of different dispersion characteristics.

where indices $p, q \in \{1, \ldots, N_s\}$ for small cells at the interface in Ω_2 for any corresponding big cell k, l at the interface in Ω_1 [see Figs. 3 and 4(a)].

We should keep in mind that the voltage incident on the interface is the same as the reflected voltage from the TLM cell from its both sides and vice versa for the reflected voltages from the interface [as shown in Fig. 4(a)]. Thus, to avoid some ambiguity, incident and reflected voltages in the large cell (k, l, m) in the left-hand side region ($\partial\Omega_1$ in Fig. 6) are

$$V^{\Omega_1}_{\text{ref},9}(k,l,m) = \tilde{u}_{2,00} \tag{23.a}$$
$$V^{\Omega_1}_{\text{ref},8}(k,l,m) = \tilde{u}_{4,00} \tag{23.b}$$
$$V^{\Omega_1}_{\text{inc},9}(k,l,m) = \tilde{v}_{2,00} \tag{23.c}$$
$$V^{\Omega_1}_{\text{inc},8}(k,l,m) = \tilde{v}_{4,00}. \tag{23.d}$$

Similarly, for incident and reflected voltages in the small cell $(p, q, m+1)$ in the right-hand side

$$V^{\Omega_2}_{\text{ref},2}(p,q,m+1) = \tilde{u}_{2,pq} \tag{24.a}$$
$$V^{\Omega_2}_{\text{ref},4}(p,q,m+1) = \tilde{u}_{4,pq} \tag{24.b}$$
$$V^{\Omega_2}_{\text{inc},2}(p,q,m+1) = \tilde{v}_{2,pq} \tag{24.c}$$
$$V^{\Omega_2}_{\text{inc},4}(p,q,m+1) = \tilde{v}_{4,pq}. \tag{24.d}$$

At this moment, one can observe the coupling between the cells at both sides of the interface in (21) and (22). This allows one to build the update equation system in both domains. Note that N_s^2 small cells $(p, q, m+1)$ with $p, q \in \{1, \ldots, N_s\}$ are adjacent to every big cell (k, l, m) in the left-hand domain. Therefore, for the rest of our derivation and without loss of generality, we will omit the big cells indices (k, l, m) and only the small cells indices (p, q) in the xy directions. Moreover, based on (10.a), (10.b), (11.b), and (12.a), any incident/reflected voltage in $\partial\Omega_2$ with indices (p, q) can be represented by the corresponding incident/reflected voltage with indices $(1, 1)$ multiplied by the corresponding space shift operator, as

$$\overline{V}^{\Omega_2,n}_{\text{inc}}(p,q) = \zeta(\text{p},\text{q})\overline{V}^{\Omega_2,n}_{\text{inc}}(1,1) \tag{25.a}$$
$$\overline{V}^{\Omega_2,n}_{\text{ref}}(p,q) = \zeta(\text{p},\text{q})\overline{V}^{\Omega_2,n}_{\text{ref}}(1,1). \tag{25.b}$$

The input voltages to cells in $\partial\Omega_1$ at the time step $(n+1)$ are the normal $\overline{V}^{\Omega_1,n+1}_{\text{inc}}$ defined in (17), except for voltages $V^{\Omega_1,n+1}_{\text{inc},8}$ and $V^{\Omega_1,n+1}_{\text{inc},9}$ that come from the right-hand side subdomain and expressed in (21) or in (23.c) and (23.d). From (17) and (21), we can observe that the connection process depends on reflected voltages from both sides of the interface, namely

TABLE II

SPACE-SHIFT OPERATORS IN THE SPECTRAL DOMAIN AND THE HILBERT SPACE FOR $\partial\Omega_2$ SUBDOMAIN (SEE FIG. 6)

Spectral domain notation	Hilbert stapce notation
$X^{\dagger} = e^{-j\chi/N_s}$	$X^{\dagger}\lvert n;p,q,m\rangle = \lvert n;p-1,q,m\rangle$
$X = e^{j\chi/N_s}$	$X\lvert n;p,q,m\rangle = \lvert n;p+1,q,m\rangle$
$Y^{\dagger} = e^{-j\eta/N_s}$	$Y^{\dagger}\lvert n;p,q,m\rangle = \lvert n;p,q-1,m\rangle$
$Y = e^{j\eta/N_s}$	$Y\lvert n;p,q,m\rangle = \lvert n;p,q+1,m\rangle$
$Z^{\dagger} = e^{\frac{j\xi}{2}(1+\frac{1}{N_s})}$	$Z^{\dagger}\lvert n;p,q,m\rangle = \lvert n;p,q,m-1\rangle$
$Z = e^{j\xi/N_s}$	$Z\lvert n;p,q,m\rangle = \lvert n;p,q,m+1\rangle$

$$\overline{V}^{\Omega_1,n+1}_{\text{inc}} = \overline{\overline{M}}(8,9)\overline{\overline{\Psi}}_{\partial\Omega_1}\overline{V}^{\Omega_1,n}_{\text{ref}} + \frac{1}{N_s}\overline{\overline{e}}\,\overline{\overline{S}}\,\overline{\overline{e}}^{T}\,\overline{\overline{P}}(8,9) \times \overline{\overline{\Psi}}_{\partial\Omega_2}\overline{V}^{\Omega_2,n}_{\text{ref}}(1,1). \tag{26.a}$$

Similarly, as done in (22.a) or (22.b), the input voltages in the subdomain $\partial\Omega_2$ for the small cell with indices (p, q) can be written

$$\overline{V}^{\Omega_2,n+1}_{\text{inc}}(p,q) = (\overline{\overline{M}}(2,4) + \gamma_x(p,q)\overline{\overline{P}}(2,2) + \gamma_y(p,q)\overline{\overline{P}}(4,4)) \times \overline{\overline{\Psi}}_{\partial\Omega_2}\overline{V}^{\Omega_2,n}_{\text{ref}}(p,q) - \frac{1}{N_s}\overline{\overline{P}}(2,4)\overline{\overline{\Psi}}_{\partial\Omega_1}\overline{V}^{\Omega_1,n}_{\text{ref}} \tag{26.b}$$

where $\gamma_x(p,q)$ and $\gamma_y(p,q)$ are defined as

$$\gamma_x(p,q) = -1 + \frac{2}{N_s}\sum_{i=1}^{N_s} e^{\frac{j2\pi\,\Delta y k_y(i-q)}{N_s}} - \frac{1}{N_s^2}\overline{\overline{e}}\,\overline{\overline{S}}\,\overline{\overline{e}}^{T}\zeta(\text{p},\text{q}) \tag{27.a}$$

$$\gamma_y(p,q) = -1 + \frac{2}{N_s}\sum_{i=1}^{N_s} e^{\frac{j2\pi\,\Delta x k_x(i-p)}{N_s}} - \frac{1}{N_s^2}\overline{\overline{e}}\,\overline{\overline{S}}\,\overline{\overline{e}}^{T}\zeta(\text{p},\text{q}) \tag{27.b}$$

where the space shift operator $\overline{\overline{\Psi}}_{\partial\Omega_2}$ is similar to $\overline{\overline{\Psi}}_{\partial\Omega_1}$ with elements given in Table II, and the 18×18 matrices $\overline{\overline{M}}(i,j)$ and $\overline{\overline{P}}(i,j)$ are operators that mask and pass the elements number i and j in operand array, respectively

$$(\overline{\overline{M}}(a,b))_{ij} = \begin{cases} 1, & \text{if } i = j \text{ and } i,j \neq \{a,b\} \\ 0, & \text{otherwise} \end{cases} \tag{28.a}$$

$$(\overline{\overline{P}}(a,b))_{ij} = \begin{cases} 1, & \text{if } i = j \text{ and } i,j = \{a,b\} \\ 0, & \text{otherwise.} \end{cases} \tag{28.b}$$

Note that $\overline{\overline{M}}(i,j)$ and $\overline{\overline{P}}(i,j)$ operate as ports that prevent or allow certain voltages to enter, respectively. Moreover, both $\gamma_x(p,q)$ and $\gamma_y(p,q)$ tend to zero as the cell dimensions Δx and Δy tend to zero.

From the definition (28), one can obtain the following two identities:

$$\overline{\overline{M}}(i,j) + \overline{\overline{P}}(i,j) = \overline{\overline{I}}_{18} \tag{29.a}$$
$$\overline{\overline{P}}(i,i) + \overline{\overline{P}}(j,j) = \overline{\overline{P}}(i,j). \tag{29.b}$$

Finally, after substituting (13), (14.a), (15), (17), and (25) in (26.a) and (26.b), respectively, we obtain

$$\overline{\overline{T}}\,\overline{V}_{\text{inc}}^{\Omega_1,n} = \overline{\overline{\Theta}}_1\overline{V}_{\text{inc}}^{\Omega_1,n} + \overline{\overline{\Theta}}_2\overline{V}_{\text{inc}}^{\Omega_2,n}(1,1) \quad (30.a)$$

$$\overline{\overline{T}}\,\overline{V}_{\text{inc}}^{\Omega_2,n}(1,1) = \overline{\overline{\Theta}}_3\overline{V}_{\text{inc}}^{\Omega_1,n} + \overline{\overline{\Theta}}_4\overline{V}_{\text{inc}}^{\Omega_2,n}(1,1) \quad (30.b)$$

where

$$\overline{\overline{\Theta}}_1 = \overline{\overline{M}}(8,9)\overline{\overline{\Psi}}_{\partial\Omega_1}(\overline{\overline{\Lambda}}_{\Omega_1}\overline{\overline{Q}}_{\Omega_1}\overline{\overline{\Gamma}}_{\Omega_1}(z) - \overline{\overline{\Phi}}_{\Omega_1}) \quad (31.a)$$

$$\overline{\overline{\Theta}}_2 = \frac{1}{N_s}\overline{\overline{e}}\,\overline{\overline{S}}\,\overline{\overline{e}}^T\overline{\overline{P}}(8,9)\overline{\overline{\Psi}}_{\partial\Omega_2}(\overline{\overline{\Lambda}}_{\Omega_2}\overline{\overline{Q}}_{\Omega_2}\overline{\overline{\Gamma}}_{\Omega_2}(z) - \overline{\overline{\Phi}}_{\Omega_2}) \quad (31.b)$$

$$\overline{\overline{\Theta}}_3 = -\frac{1}{\zeta(p,q)N_s}\overline{\overline{P}}(2,4)\overline{\overline{\Psi}}_{\partial\Omega_1}(\overline{\overline{\Lambda}}_{\Omega_1}\overline{\overline{Q}}_{\Omega_1}\overline{\overline{\Gamma}}_{\Omega_1}(z) - \overline{\overline{\Phi}}_{\Omega_1}) \quad (31.c)$$

$$\overline{\overline{\Theta}}_4 = (\overline{\overline{M}}(2,4) + \gamma_x(p,q)\overline{\overline{P}}(2,2) + \gamma_y(p,q)\overline{\overline{P}}(4,4)) \times \overline{\overline{\Psi}}_{\partial\Omega_2}(\overline{\overline{\Lambda}}_{\Omega_2}\overline{\overline{Q}}_{\Omega_2}\overline{\overline{\Gamma}}_{\Omega_2}(z) - \overline{\overline{\Phi}}_{\Omega_2}). \quad (31.d)$$

From (30.a) and (30.b), we can obtain the dispersion relation for the case of meshing per block with global time step for cells at the interface in $\partial\Omega_1$ and $\partial\Omega_2$ (as shown in Fig. 6). The necessary condition for (30) to have a nontrivial solution is

$$\det\left(\begin{bmatrix} \overline{\overline{T}} - \overline{\overline{\Theta}}_1 & -\overline{\overline{\Theta}}_2 \\ -\overline{\overline{\Theta}}_3 & \overline{\overline{T}} - \overline{\overline{\Theta}}_4 \end{bmatrix}\right) = 0. \quad (32)$$

The resulting expression (32) is the dispersion relation that links the time step Δt, mesh sizes $(\Delta x, \Delta y, \Delta z)$, subgridding ratio N_s, the media properties of the propagating medium $\overline{\overline{\Gamma}}$, and the direction of propagation $\vec{k}$.

To simplify the analysis, one can decouple (30.a) and (30.b) as

$$\overline{\overline{T}}\,\overline{V}_{\text{inc}}^{\Omega_1,n} = (\overline{\overline{\Theta}}_2(\overline{\overline{T}} - \overline{\overline{\Theta}}_4)^{-1}\overline{\overline{\Theta}}_3 + \overline{\overline{\Theta}}_1)\overline{V}_{\text{inc}}^{\Omega_1,n} \quad (33.a)$$

$$\overline{\overline{T}}\,\overline{V}_{\text{inc}}^{\Omega_2,n}(1,1) = (\overline{\overline{\Theta}}_3(\overline{\overline{T}} - \overline{\overline{\Theta}}_1)^{-1}\overline{\overline{\Theta}}_2 + \overline{\overline{\Theta}}_4)\overline{V}_{\text{inc}}^{\Omega_2,n}(1,1). \quad (33.b)$$

Thus, we can have two separate dispersion relations for cells at both sides of the interface $\partial\Omega_1$ and $\partial\Omega_2$, respectively

$$\det(\overline{\overline{T}} - \overline{\overline{\Theta}}_1 - \overline{\overline{\Theta}}_2(\overline{\overline{T}} - \overline{\overline{\Theta}}_4)^{-1}\overline{\overline{\Theta}}_3) = 0 \quad (34.a)$$

$$\det(\overline{\overline{T}} - \overline{\overline{\Theta}}_4 - \overline{\overline{\Theta}}_3(\overline{\overline{T}} - \overline{\overline{\Theta}}_1)^{-1}\overline{\overline{\Theta}}_2) = 0. \quad (34.b)$$

From (31.c) and (31.d), one can observe the dependence of the matrices $\overline{\overline{\Theta}}_3$ and $\overline{\overline{\Theta}}_4$ on the small cell indices (p,q) in $\partial\Omega_2$. Therefore, when solving (34), we can expect different dispersion characteristics for small cells in $\partial\Omega_2$ in different positions $(p,q)\forall \text{p, q} \in \{1,\ldots,\text{N}_\text{s}\}$.

One interesting point to observe is that, as mesh sizes and time step go to zero, all three-connection matrices, namely, $\overline{\overline{\Psi}}$ in the uniform meshing case (1), and $\overline{\overline{\Psi}}_{\partial\Omega_1}$ and $\overline{\overline{\Psi}}_{\partial\Omega_2}$ in Tables I and II, converge to the same value (because all elements in Tables I and II will tend to unity)

$$\lim_{\Delta x,\Delta y,\Delta z\to 0}\overline{\overline{\Psi}} = \lim_{\Delta x,\Delta y,\Delta z\to 0}\overline{\overline{\Psi}}_{\partial\Omega_1} = \lim_{\Delta x,\Delta y,\Delta z\to 0}\overline{\overline{\Psi}}_{\partial\Omega_2}. \quad (35.a)$$

This means that the combined processes of connection and the media–fields' interaction in the right-hand expressions

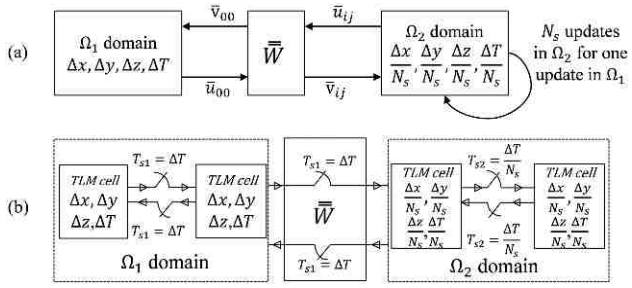

Fig. 7. (a) Block diagram of the interaction between the two subdomains Ω_1 and Ω_2. (b) Spatiotemporal interface with local time step (multirate system).

of (33.a) and (33.b) tend also to

$$\lim_{\Delta x,\Delta y,\Delta z,\Delta t\to 0}\overline{\overline{\Psi}}(\overline{\overline{\Lambda}}\,\overline{\overline{\Gamma}}(z)\overline{\overline{Q}} - \overline{\overline{\Phi}}) = \lim_{\Delta x,\Delta y,\Delta z,\Delta t\to 0}\overline{\overline{\Theta}}_2(\overline{\overline{T}} - \overline{\overline{\Theta}}_4)^{-1}\overline{\overline{\Theta}}_3 + \overline{\overline{\Theta}}_1 = \lim_{\Delta x,\Delta y,\Delta z,\Delta t\to 0}\overline{\overline{\Theta}}_3(\overline{\overline{T}} - \overline{\overline{\Theta}}_1)^{-1}\overline{\overline{\Theta}}_2 + \overline{\overline{\Theta}}_4. \quad (35.b)$$

The term $\overline{\overline{\Psi}}(\overline{\overline{\Lambda}}\,\overline{\overline{\Gamma}}(z)\overline{\overline{Q}} - \overline{\overline{\Phi}})$ in (35.b) or in (1) was shown to converge to the continues form of Maxwell's equations as the cell dimensions and the time step go to zero [25]. This indicates that the dispersion relations (34.a) and (34.b) for the case of meshing per block with a finite subgridding ratio N_s eventually (as meshes become very fine) converge to the same dispersion relations as uniform gird in (1). This shows that the limiting case for meshing per block with a global time step converges to the continuous model of Maxwell's equations as mesh sizes tend to zero.

One can observe that, wherever there is an interface between two subdomains of different mesh sizes, there are four regions to consider for dispersion analysis, namely, the subdomain Ω_1, the cells at the interface in $\partial\Omega_1$, the subdomain Ω_2, and the cells touching the interface in $\partial\Omega_2$ (as shown in Fig. 6).

The numerical dispersion error is accumulated as EM waves propagate in the discrete computational domain. Therefore, the maximum dispersion error among the regions $\Omega_1, \partial\Omega_1$, Ω_2, and $\partial\Omega_2$ will give us the upper threshold of numerical dispersion error in the entire domain shown in Fig. 6.

C. Dispersion Equations for the Cells at the Interface Between Two Subdomains of Different Mesh Sizes With Local Time Step

In this scenario, the interface between the two subdomains Ω_1 and Ω_2 is composed of two processes, namely, the spatial interface that we have seen in Section II-B and the temporal interface. The temporal interface (shown in Fig. 7) indicates that the subdomain Ω_2 that operates at $\Delta t = \Delta T/N_s$ needs to perform N_s fields' updates for a single update in the subdomain Ω_1 (to keep the entire domain synchronized).

This temporal aspect of using local time step can be better understood by considering a simpler case of a multirate filter with feedback and shows the new stability condition. The analog filter shown in Fig. 8(a) is discretized twice; first, into the single-rate digital filter shown in Fig. 8(b); then, into a multirate filter with up and down samplers, as shown

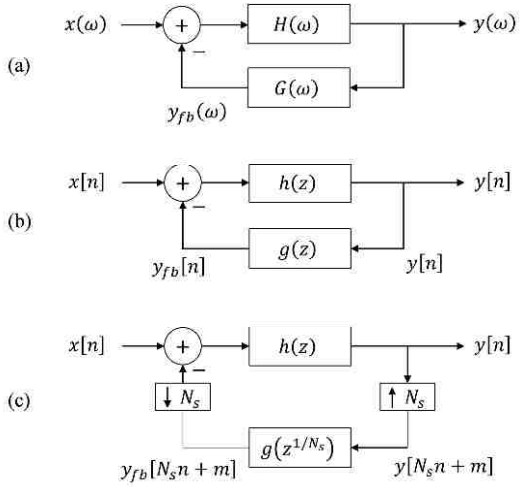

Fig. 8. (a) Analog filter with a negative feedback. (b) Discretization of the analog filter with a single global sampling rate. (c) Discretization of the analog filter with different sampling rates.

in Fig. 8(c). Usually, for a single rate filter [see Fig. 8(b)], the stability criterion states that the poles of the overall transfer function of the filter (36.a) must not be outside the unit circle in the z-domain, with $z = e^{j\omega\Delta T}$ [39] (a kind remark for the reader to distinguish between z in this context of z transform and z-domain, and the z-axis shown in Figs. 1, 5, and 6)

$$K_1(z) = \frac{H(z)}{1 + H(z)G(z)}. \tag{36.a}$$

However, for the multirate filter shown in Fig. 8(c), the transfer function is dependent on the ratio N_s, and it is given by [39]

$$K_2(z) = \frac{H\left(z^{1/Ns}\right)}{1 + \sum_{k=1}^{Ns} H\left(z^{\frac{1}{Ns}} e^{\frac{j2\pi k}{Ns}}\right) G\left(z^{\frac{1}{Ns}} e^{\frac{j2\pi k}{Ns}}\right)}. \tag{36.b}$$

Again, the stability criteria for the new system require that poles of the new transfer function $K_2(z)$ should be inside the unit circle. One might mistakenly suppose that the up sampler and the down sampler in Fig. 8(c) eliminate each other effect, and a similar stability condition for the single-rate and multirate systems is required. However, as we can notice from (36.a) and (36.b), both systems are different since the latter depends on N_s and their stability criteria are different as well [39].

This brings us back to the case of multirate TLM numerical simulation with a local time step; we cannot ensure the stability of the multirate TLM model by ensuring the stability of each subdomain separately.

To develop the dispersion equations for the system shown by Fig. 7(a) and (b), we start by the following observation: cells adjacent to the interface on the right-hand side ($\partial\Omega_2$) see incident voltages coming from the left-hand side constant during ΔT or N_s samples. In other words, the temporal interface from $\partial\Omega_1$ to $\partial\Omega_2$ behaves like a zero-order hold filter.

Similar to the time-shift operator (13.a), we define the new local time-shift operators ($\overline{\overline{T}}^{\Omega_1}$ and $\overline{\overline{T}}_m^{\Omega_2}$) in subdomains $\partial\Omega_1$ and $\partial\Omega_2$, respectively, as

$$\overline{\overline{T}}^{\Omega_1} = e^{j\omega\Delta T}\overline{\overline{I}}_{18} \tag{37.a}$$

$$\overline{\overline{T}}_m^{\Omega_2} = e^{j\omega\Delta T}\overline{\overline{I}}_{18}\overline{\overline{P}}(2,4)\delta(m) + e^{j\omega\Delta t}\overline{\overline{I}}_{18}\overline{\overline{M}}(2,4). \tag{37.b}$$

At this moment, we need to introduce a second temporal index $m \in \{0, \ldots, N_s - 1\}$ for the local updates in Ω_2. ΔT is the CFL limit in Ω_1, and Δt is the corresponding CFL limit in Ω_2. Note that, in a homogeneous medium, $\Delta t = \Delta T/N_s$, and finally, $\delta(m)$ is the discrete delta function. $\delta(m)$ is used to model the fact that, at $m = 0$, a new sample comes from the left-hand side domain Ω_1 and remains constant for the subsequent small time steps $0 < m \leq N_s - 1$.

Because incident voltages coming from Ω_1 are updated only when $m = 0$ and the other voltages inside the mesh Ω_2 keep updating for every m, one can expect that the dispersion equation in Ω_2 depends on m. In analogy with (30) and for all small time steps $0 \leq m \leq N_s - 1$, voltage update equations in the subdomains Ω_1 and Ω_2 are given by, respectively

$$\overline{\overline{T}}^{\Omega_1}\overline{V}_{\text{inc}}^{\Omega_1,n} = \overline{\overline{\Theta}}_1\overline{V}_{\text{inc}}^{\Omega_1,n} + \overline{\overline{\Theta}}_2\overline{V}_{\text{inc}}^{\Omega_2,n,0}(1,1) \tag{38.a}$$

$$\overline{\overline{T}}_m^{\Omega_2}\overline{V}_{\text{inc}}^{\Omega_2,n,m}(1,1) = \overline{\overline{\Theta}}_3\overline{V}_{\text{inc}}^{\Omega_1,n} + \overline{\overline{\Theta}}_4\overline{V}_{\text{inc}}^{\Omega_2,n,m}(1,1). \tag{38.b}$$

Relation (38.a) means that voltages are updated once every ΔT in the left-hand side subdomain Ω_1, while (38.b) indicates that voltages in the fine resolution domain are updated every $\Delta T/N_s$. By decoupling (38.a) and (38.b), we obtain

$$\overline{\overline{T}}^{\Omega_1}\overline{V}_{\text{inc}}^{\Omega_1,n} = \left(\overline{\overline{\Theta}}_2\left(\overline{\overline{T}}_0^{\Omega_2} - \overline{\overline{\Theta}}_4\right)^{-1}\overline{\overline{\Theta}}_3 + \overline{\overline{\Theta}}_1\right)\overline{V}_{\text{inc}}^{\Omega_1,n} \tag{39.a}$$

$$\overline{\overline{T}}_m^{\Omega_2}\overline{V}_{\text{inc}}^{\Omega_2,n,m}(1,1) = \left(e^{-\frac{j\omega\Delta Tm}{N_s}}\overline{\overline{\Theta}}_3(\overline{\overline{T}}^{\Omega_1} - \overline{\overline{\Theta}}_1)^{-1}\overline{\overline{\Theta}}_2 + \overline{\overline{\Theta}}_4\right) \times \overline{V}_{\text{inc}}^{\Omega_2,n,m}(1,1). \tag{39.b}$$

From the above equations, dispersion relations for cells at both sides of the interface can be obtained. Thus, for $\partial\Omega_1$, we obtain

$$\det\left[\overline{\overline{T}}^{\Omega_1} - \left(\overline{\overline{\Theta}}_2\left(\overline{\overline{T}}_0^{\Omega_2} - \overline{\overline{\Theta}}_4\right)^{-1}\overline{\overline{\Theta}}_3 + \overline{\overline{\Theta}}_1\right)\right] = 0. \tag{40.a}$$

However, for cells in the interface at the right-hand subdomain $\partial\Omega_2$, the dispersion relation depends also on the small time index m

$$\det\left[\overline{\overline{T}}_m^{\Omega_2} - \left(e^{-\frac{j\omega\Delta Tm}{N_s}}\overline{\overline{\Theta}}_3(\overline{\overline{T}}^{\Omega_1} - \overline{\overline{\Theta}}_1)^{-1}\overline{\overline{\Theta}}_2 + \overline{\overline{\Theta}}_4\right)\right] = 0. \tag{40.b}$$

Now, if we are interested in the overall dispersion relation in the $\partial\Omega_2$ cells over N_s small time steps, one can use (39.b) to obtain

$$\prod_{m=0}^{N_s-1}\overline{\overline{T}}_m^{\Omega_2} - \prod_{m=0}^{N_s-1}\left(e^{-\frac{j\omega\Delta Tm}{N_s}}\overline{\overline{\Theta}}_3(\overline{\overline{T}}^{\Omega_1} - \overline{\overline{\Theta}}_1)^{-1}\overline{\overline{\Theta}}_2 + \overline{\overline{\Theta}}_4\right) = 0. \tag{41.a}$$

From (37.a) and (37.b), one can easily verify that

$$\overline{\overline{T}}^{\Omega_1} = \left(\prod_{m=0}^{N_s-1}\overline{\overline{T}}_m^{\Omega_2}\right). \tag{41.b}$$

Based on (40) and (41.a), one can compute the maximum mesh size and/or the necessary meshing ratio N_s that guarantee the acceptable level of numerical dispersion set *a priori*.

Again, as in the case of global time step in (35.b), the discrete TLM model with local time step in the coarse mesh region converges to the continues Maxwell's model as both mesh dimensions and time step tend to zero

$$\lim_{\Delta x,\Delta y,\Delta z,\Delta T\to 0} \overline{\overline{\Psi}}(\overline{\overline{\Lambda}}\,\overline{\overline{\Gamma}}(z)\overline{\overline{Q}}-\overline{\overline{\Phi}}) = \lim_{\Delta x,\Delta y,\Delta z,\Delta T\to 0} \left(\overline{\overline{\Theta}}_2\left(\overline{\overline{T}}_0^{\Omega_2}-\overline{\overline{\Theta}}_4\right)^{-1}\overline{\overline{\Theta}}_3+\overline{\overline{\Theta}}_1\right). \quad (42.a)$$

However, for the small cells' region in $\partial\Omega_2$, where fields are updated N_s times for every one update in the coarse region, one can notice that

$$\lim_{\Delta x,\Delta y,\Delta z,\Delta T\to 0} \overline{\overline{\Psi}}(\overline{\overline{\Lambda}}\,\overline{\overline{\Gamma}}(z)\overline{\overline{Q}}-\overline{\overline{\Phi}}) \neq \lim_{\Delta x,\Delta y,\Delta z,\Delta T\to 0} \prod_{m=0}^{N_s-1}\left(e^{-\frac{j\omega\Delta Tm}{N_s}}\overline{\overline{\Theta}}_3(\overline{\overline{T}}^{\Omega_1}-\overline{\overline{\Theta}}_1)^{-1}\overline{\overline{\Theta}}_2+\overline{\overline{\Theta}}_4\right). \quad (42.b)$$

This means that, as the mesh sizes get smaller and smaller, the dispersion matrix of fine region cells does not converge to the continuous dispersion matrix derived from Maxwell's equations [25]. This shows that the temporal interface produces an artifact that makes the update equation deviate from Maxwell's equations. For future research, one can think of techniques to correct the model (39) to be consistent with Maxwell equations while keeping the local time step.

III. Stability Conditions for TLM Unstructured Meshing

The stability condition of a time-domain numerical scheme is a direct consequence of the dispersion model. More specifically, it is to find out the maximum time step beyond which the numerical scheme becomes unstable [25], [29], [40]. This maximum time step Δt normally depends on mesh sizes $(\Delta x, \Delta y, \Delta z)$, the subgridding ratio N_s, and the media properties of the propagating medium represented by the correction matrix $\overline{\overline{\Gamma}}(z)$.

Recall that a discrete time-varying system is defined as [40]

$$\overline{\chi}_{n+1}=\overline{\overline{A}}\,\overline{\chi}_n \quad (43)$$

where $\overline{\overline{A}}$ is the state transition matrix. The necessary condition for the stability of (43) is that all eigenvalues of $\overline{\overline{A}}$ should be within the unit circle [25], [30]. As we did for dispersion analysis, we will study both cases separately, namely, global and local time steps:

A. Block Meshing With Global Time Step

From (33), the state transition matrices can be identified

$$\overline{\overline{A}}_1=(\overline{\overline{\Theta}}_2(\overline{\overline{T}}-\overline{\overline{\Theta}}_4)^{-1}\overline{\overline{\Theta}}_3+\overline{\overline{\Theta}}_1) \quad (44.a)$$

$$\overline{\overline{A}}_2=(\overline{\overline{\Theta}}_3(\overline{\overline{T}}-\overline{\overline{\Theta}}_1)^{-1}\overline{\overline{\Theta}}_2+\overline{\overline{\Theta}}_4). \quad (44.b)$$

Both matrices should have eigenvalues inside the unit circle to ensure stability [25], [40]

$$|\lambda_{i,A_1}|\le 1 \quad |\lambda_{i,A_2}|\le 1 \quad \forall i\in\{1,\ldots,18\}. \quad (45)$$

One should keep in mind that Δt is involved in both matrices. Hence, one can find the maximum Δt after which the condition (45) is no longer satisfied.

For simple media defined by their permittivity ε_r and permeability μ_r, one can use (44) and (45) to obtain the maximum global time step that guarantees stability in block meshing with N_s subgridding ratio, which is defined as

$$\Delta T=\frac{\sqrt{\varepsilon_r\mu_r}}{N_s c_0\sqrt{\left(\frac{1}{\Delta x}\right)^2+\left(\frac{1}{\Delta y}\right)^2+\left(\frac{1}{\Delta z}\right)^2}}. \quad (46)$$

However, if the computational domain is composed of heterogeneous media, the time step that guarantees stability is the minimum CFL limit in the entire computational domain; in other words

$$\Delta T_{\Omega_1}=\min\left(\frac{\sqrt{\varepsilon_r(I,J,K)\mu_r(I,J,K)}}{c_0\sqrt{\left(\frac{1}{\Delta x}\right)^2+\left(\frac{1}{\Delta y}\right)^2+\left(\frac{1}{\Delta z}\right)^2}}\right) \quad \forall(I,J,K)\ \text{cells}\ \in\Omega_1 \quad (47.a)$$

$$\Delta T_{\Omega_2}=\min\left(\frac{\sqrt{\varepsilon_r(i,j,k)\mu_r(i,j,k)}}{N_s c_0\sqrt{\left(\frac{1}{\Delta x}\right)^2+\left(\frac{1}{\Delta y}\right)^2+\left(\frac{1}{\Delta z}\right)^2}}\right) \quad \forall(i,j,k)\ \text{cells}\ \in\Omega_2. \quad (47.b)$$

Thus, the maximum time step that guarantees stability in the computational domain is given by

$$\Delta T=\min(\Delta T_{\Omega_1},\Delta T_{\Omega_2}). \quad (47.c)$$

B. Block Meshing With Local Time Step

Similarly, from (39.a) and (41.a), the state transition matrices for the case of local time step are defined as

$$\overline{\overline{B}}_1=(\overline{\overline{\Theta}}_2(\overline{\overline{T}}_0^{\Omega_2}-\overline{\overline{\Theta}}_4)^{-1}\overline{\overline{\Theta}}_3+\overline{\overline{\Theta}}_1) \quad (48.a)$$

$$\overline{\overline{B}}_2=\prod_{m=0}^{N_s-1}\left(e^{-\frac{j\omega\Delta Tm}{N_s}}\overline{\overline{\Theta}}_3(\overline{\overline{T}}^{\Omega_1}-\overline{\overline{\Theta}}_1)^{-1}\overline{\overline{\Theta}}_2+\overline{\overline{\Theta}}_4\right). \quad (48.b)$$

Both matrices should have eigenvalues inside or at the boundaries of the unit circle to ensure stability [25], [40]

$$|\lambda_{i,B_1}|\le 1 \quad |\lambda_{i,B_2}|\le 1 \quad \forall i\in\{1,\ldots,18\}. \quad (49)$$

Again, the objective is to find the maximum Δt for which the condition (49) is fulfilled. Note that an eigenvalue analytical general expression for arbitrary *Ns* is very cumbersome for the local time step. However, all involved matrices in the stability issue are analytically derived. They are ready to test for stability, given a *Ns* subgridding ratio, by simple matrices' eigenvalue computation.

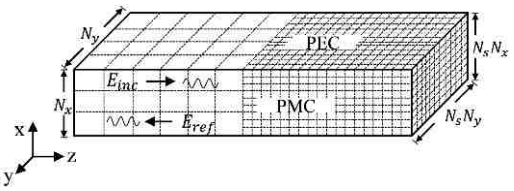

Fig. 9. Parallel-plate wavegude, discretized with block meshing.

IV. Results and Discussion

In this section, three experiments that use block meshing are presented to validate the proposed dispersion and stability model approach. The first two experiments are concerned with the dispersion analysis and to show the effects of different subgridding ratios on the simulation accuracy. In the third experiment, we study the resolution enhancement and the dispersion error for the resonant modes in a rectangular cavity. In addition, we study the stability for both local and global time steps. Since our main interest is the geometrical and discretization aspect, a homogeneous medium (free space) was used for the three experiments. Cubic cells were also used in all experiments as it is optimum in terms of maximum time step and minimum dispersion. However, the proposed approach is also valid for parallelepipedic cells with arbitrary aspect ratios. All codes were implemented using FORTRAN 95 language and parallelized using the MPI library. All TLM simulations were conducted on Linux operating system, with Intel Xeon E5 - 2697v3, 2.6-GHz processor.

A. TEM Mode Propagation in a Parallel-Plate Waveguide

In this experiment, we study the wave propagation in a parallel-plate waveguide, as shown in Fig. 9. To show the impact of using meshing per block, we compute (with a TLM simulation) the reflection coefficient from the spatial interface between the two subdomains as a function of frequency and the subgridding ratio N_s. Then, we compute the reflection coefficient predicted by the analytical dispersion model presented in this article. For that case, we will consider that every discretization (mesh size and time step) can be equivalent to a slight modification of the electric permittivity of the discretized medium (free space in our experiment), namely, the regions $\Omega_1, \partial\Omega_1$, Ω_2, and $\partial\Omega_2$. These slight apparent changes in permittivity are computed using (34). Therefore, one can theoretically compute the reflection from the interface between the coarse and fine meshes of Fig. 9.

The structure was excited by a modulated-Gaussian pulse ($f_0 = 2.5$ GHz, $t_o = 9.17$ ns, and $\sigma = 1.65$ ns). The waveguide is terminated by the free space η_o impedance as an absorbing boundary condition. Global time step is used, with a mesh size $\Delta x = 5.5$ mm in coarse region (see Fig. 9), which corresponds to $\lambda_{\min}/20$.

As shown in Fig. 10, the reflection coefficient increases with frequency because the numerical dispersion increases. In addition, the dispersion increases when the subgridding ratio N_s increases. Note that (34) was solved numerically using the bisection method. Moreover, to simplify the theoretical computation of the reflection coefficient, the apparent permittivity in the layer $\partial\Omega_2$ (34) was obtained only for the pair

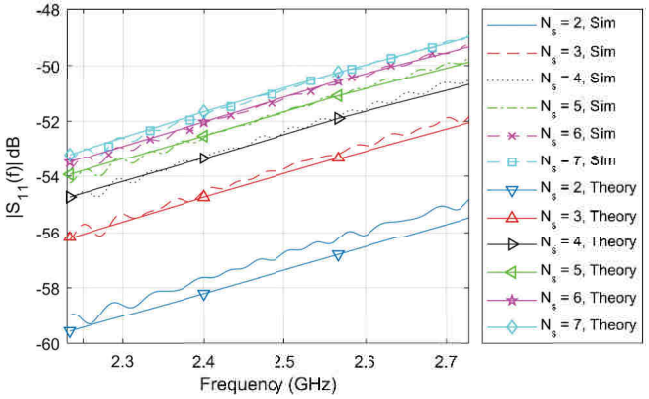

Fig. 10. Reflection coefficient between the coarse region and the fine mesh in the parallel-plate waveguide [see Fig. 9] and full-wave TLM simulations versus theoretical model (34).

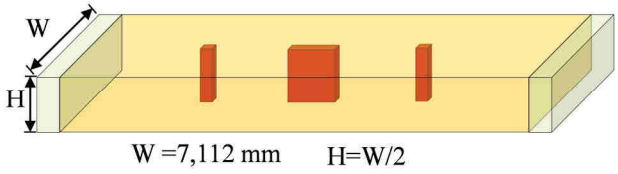

Fig. 11. Rectangular waveguide bandpass filter with vias.

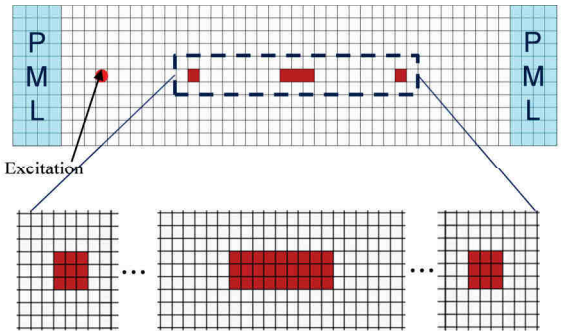

Fig. 12. Top view of the waveguide shown in Fig. 12, discretized nonuniformly with meshing per block.

$(p = 1, q = 1)$, and this value was used in all small cells in $\partial\Omega_2$. However, there are slight differences in dispersion characteristics for different small cells $(p, q) \forall p, q \in \{1, \ldots, N_s\}$. This explains the small differences between the reflection coefficient curves obtained theoretically and the ones obtained using the full-wave TLM simulations shown in Fig. 10.

Note that, Ijjeh *et al.* [41] tested the dispersion characteristics in the TLM domain with subgridding and global time experimentally using real simulations (see Figs. 9 and 10), without any comparison with a theoretical model. However, (34) allows one to compute the dispersion levels without the necessity to conduct TLM simulations. Moreover, close levels of the reflection coefficient from the interface as predicted using the model (34) compared to real simulations.

B. Dispersion Error in the S-Parameters of a Rectangular Waveguide With Iris

In this experiment, we investigate the coarseness error that occurs around discontinuities, in this case, the iris shown

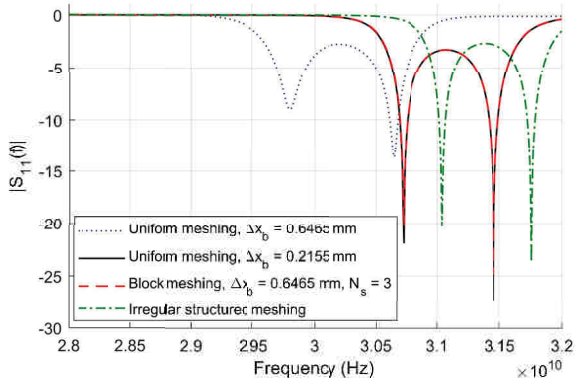

Fig. 13. Reflection coefficient of a lossless microwave filter, comparisons between coarse meshing, fine meshing, meshing per block, and structured irregular meshing.

TABLE III
SIMULATION TIME AND MEMORY REQUIREMENTS FOR EXPERIMENTS SHOWN IN FIG. 13

	Coarse meshing	Irregular structured meshing	Block meshing ($N_s = 3$)	Fine meshing (referenc)
CPU-time	0m45s	1h01m12s	5m37s	20m13s
N_{cells}	7920	71280	59400	213840

in Figs. 11 and 12. It shows the effectiveness of using block meshing to reduce this type of error.

The microwave filter shown in Fig. 11 is discretized with block meshing, with an increased resolution around the iris (see Fig. 12). The time excitation was a modulated-Gaussian pulse ($f_0 = 30$ GHz, $t_o = 6.47$ ns, and $\sigma = 0.32$ ns). The waveguide is terminated by a perfectly matched layer (PML) at both ends. The PML layer is terminated by free space η_o impedance boundary condition to enhance the PML absorbing properties. The global time step is used.

The relevance of using fine mesh around discontinuities stems from the fact that evanescent modes generated there should be accurately reproduced as they represent reactive power stored nearby, and they have some very sensitive impact on the scattering parameters. Generally, there is no strategy to determine the fine cell domain extend. However, if physical guidelines cannot be applied, convergence tests should be performed.

Results in Fig. 13 show some relevant observations. First, one can see practically no difference between meshing per block and fine-mesh simulations. This indicates that the dispersion generated by the block-meshing algorithm is negligible. Then, we see that, using coarse mesh (yet, $\Delta x \approx (\lambda_{\min}/17)$), one obtains inaccurate results. This shows that the traditional rule of using ten cells per wavelength is valid only in presence of smooth geometries (no discontinuities) and simple media. Finally, when using meshing per block to enhance the spatial discretization around discontinuities, one can obtain some substantial gain in terms of required memory and CPU time, as shown in Table III. For comparison, we conducted the same experiment with irregularly structured meshing to enhance

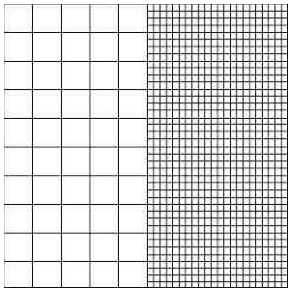

Fig. 14. Cross section of a rectangular cavity discretized with block meshing.

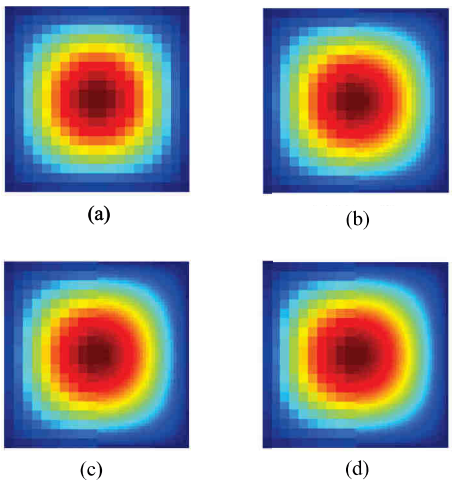

Fig. 15. E_z field distributions for the TM_{110} mode for different N_s's [41]. (a) $N_s = 1$. (b) $N_s = 2$. (c) $N_s = 3$. (d) $N_s = 4$.

the resolution around the discontinuities in Fig. 11. However, the CPU time was extremely large even compared to uniform fine resolution (see Table III). This is because, when the cell deviates from the cubic shape (aspect ratio $\neq 1$), the maximum time step rapidly decreases. For comparison, it was 1.08 ps for the large cubic cells, 0.36 ps for the small cubic cells, and 0.12 ps for the parallelepipedic cells used in the irregularly structured meshing of dimensions: 0.2155 mm $\times$ 0.2155 mm $\times$ 0.6465 mm.

C. Dispersion of Resonant Modes in a Cubic Cavity

In this experiment, we study the first TE and TM resonant modes in a cubic cavity. To investigate the effects of block meshing on resonant mode distribution and associated resonant frequencies accuracy, the cavity is half-meshed with a coarse mesh and the other half with fine mesh, as shown in Fig. 14. A narrowband modulated Gaussian pulse centered at the theoretical resonant frequency is used for excitation. This allows one to excite only the mode of interest. For both TE and TM modes, a mesh size of $\lambda/40$ was used in the coarse region, where λ is the free-space wavelength. This eliminates the effects of numerical dispersion in any of the separated regions (the numerical error is $< 0.01\%$). Therefore, we can investigate the dispersion error due to the mesh interface only.

In Fig. 15, we show the E_z field distribution in the x–y cross section of the cavity for the TM_{110} resonant mode. One can observe that, by increasing the subgridding ratio N_s,

TABLE IV

RELATIVE ERROR IN RESONANT FREQUENCY FOR THE TM_{110} AND THE DISPERSION ERROR FOR CELLS AT THE INTERFACE BETWEEN BOTH SUBDOMAINS

	Relative error in resonant frequency	Dispersion error	
Ns	TM_{110} mode	$\partial\Omega_1$	$\partial\Omega_2$
2	0.63 %	0,88 %	0,82 %
3	0.96 %	1,24 %	1,16 %
4	1.27 %	1,46 %	1,34 %
5	1.41 %	1,50 %	1,45 %

TABLE V

RELATIVE ERROR IN RESONANT FREQUENCY FOR THE TE_{101} AND THE DISPERSION ERROR FOR CELLS AT THE INTERFACE BETWEEN BOTH SUBDOMAINS

	Relative errer	Dispersion error	
Ns	TE_{101} mode	$\partial\Omega_1$	$\partial\Omega_2$
2	0.09 %	0.08 %	<0.01 %
3	0.12 %	0.11 %	<0,01 %
4	0.13 %	0.13 %	<0.01 %
5	0.14 %	0.15 %	<0.01 %

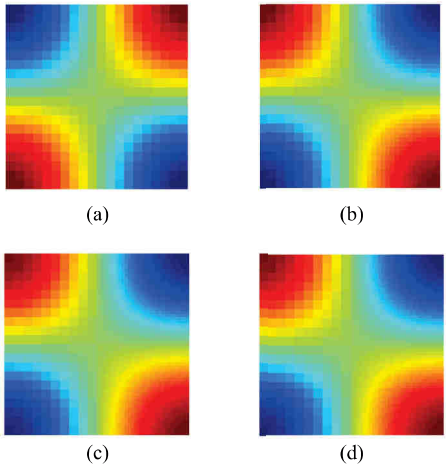

Fig. 16. H_z field distributions for the TE_{101} mode for different N_s's [41]. (a) $N_s = 1$. (b) $N_s = 2$. (c) $N_s = 3$. (d) $N_s = 4$.

the resolution in the right-hand half increases. Theoretically, this TM mode can be seen as a plane wave propagating at an angle of 45° in the xy plane. This permits us to study a scenario of the oblique incidence of the plane wave hitting the interface between both subdomains.

To compute the dispersion error in both regions, (34.a) and (34.b) were solved simultaneously to obtain a k-vector in both domains. The error in the k-vector as compared to the theoretical value of $|\vec{k}| = c_o/(\omega\sqrt{\varepsilon_r \mu_r})$ is directly proportional to the error in the resonant frequency, as shown in Table IV. The system (34) is a nonlinear one of high order in general as it is the determinant of an 18×18 matrix containing exponent expressions. Thus, it was solved numerically using the bisection method [42]. The starting point of the search was chosen to be the theoretical wavenumber value k; the objective of the program is to minimize the absolute value of the determinants in (34.a) and (34.b).

Similarly, in Fig. 16, we show the H_z field distribution in the x–y cross section of the cavity for the TE_{101} resonant mode. One can also observe that, by increasing the subgridding ratio N_s, the resolution in the right-hand half increases.

Table V shows the dispersion error computed at both sides of the interface $\partial\Omega_1$ and $\partial\Omega_2$ and the corresponding relative error in the TE_{101} resonant mode. One can notice that the impact of numerical dispersion is minimal as compared to the previous case of TM_{110}, as shown in Table IV. The reason is that the current TE_{101} mode is composed of a plane wave propagating in the x-direction where the incidence is normal to the interface between both subdomains of different mesh ratios.

Dispersion from the interface has also an anisotropic character, i.e., it depends on the wave propagation direction that is modeled. This is shown by comparing Tables IV and V as the error is substantially higher for the TM_{110} case than for the TE_{101} one. In the first case, waves travel at an angle, which is 45° with the interface, while they do it perpendicularly for the second case. One can also notice that the error increases with the mesh ratio N_s. This is indeed the motivation for the dispersion study presented in this article: It shows that some additional dispersion is generated by the interface and growths with N_s. However, it remains low and block meshing still brings some substantial computer cost reduction.

The work presented in [41] showed the dispersion in the TLM domain with subgridding and global time step experimentally using real simulations, with no results from a theoretical model. However, the dispersion model (34) allows one to compute the dispersion levels without the necessity to run TLM simulations. Moreover, we were able to obtain similar levels of dispersion error as predicted by the upper dispersion limit obtained using (34).

For the stability study, we compare the cavity experiment when using local and global time steps. The structure of Fig. 14 was excited by a Dirac impulse (to excite all possible propagating modes) for the case $N_s = 4$. In Fig. 17, we can see that, while up to about 700 iterations responses are identical, the one using the local time step clearly produces some growing instability beyond that time. An analysis in terms of eigenvalues to explain the observed behaviors is given in the following.

The maximum eigenvalue of (48.b) was $\max(|\lambda_{i,B_2}|) = 1.0 + 4.37 \times 10^{-3}$. Thus, instability occurs, as shown in Fig. 17(b). However, one can prevent this instability by applying the average-filtering technique proposed in [14]. The reason is that this averaging technique behaves as a very weak damper that relocates the eigenvalues of (48) inside the unit circle. For instance, if we apply this filter to the case shown in Fig. 17(b), the maximum eigenvalue of (48.b) becomes $\max(|\lambda_{i,B_2}|) = 1.0 - 9.053 \times 10^{-6}$. On the other hand, when the global time step is used, no sign of instability was observed even up to two million iterations. That was verified by computing the eigenvalues in (49) and ensure that all of them are within the unit circle (several of them are on the

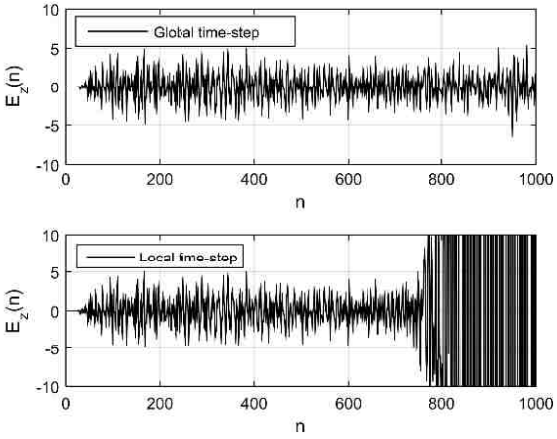

Fig. 17. E_z field evolution in time when the cavity of Fig. 14 is excite by a Dirac impulse, global time step versus local time step ($N_s = 4$).

boundaries of the circle, i.e., $\max(|\lambda_{\mathrm{i,A_1}}|) = \max(|\lambda_{\mathrm{i,A_2}}|) = 1.0$) if the global time step is not larger than the smallest CFL limit in both domains.

V. Conclusion

In this article, we presented a mathematical formulation for dispersion relationships of a plane wave propagating in an unstructured Cartesian mesh with block meshing. This model permits us to use adequate mesh sizes that guarantee a tolerable level of numerical dispersion and the corresponding time step that ensures stability. Therefore, computational expenditures can be minimized. The alternative to the proposed approach is to perform convergence tests/tests to ensure a negligible level of dispersion error. These convergence tests usually require much more computational resources than using the proposed approach. Moreover, this model shows that the dispersion error in the computational domain with block meshing can largely exceed the dispersion error in every subdomain taken separately. In other words, the dispersion analysis at the interface between different subdomains with different mesh sizes is necessary to guarantee a tolerable level of numerical dispersion. The proposed technique also shows the origins of the instability observed when the local time step is used with the block-meshing technique by using an eigenvalue analysis. Moreover, it was shown that, at the interface between two regions with different mesh sizes, the algorithm does not tend to the continuous model when both mesh size and time step tend to zero. This knowledge can be useful in investigating new methods for correctly modifying the update equations at the interface to prevent the instability associated with the local time step.

Acknowledgment

This work benefited from access to CINES computing resources through the 2019-A0060505122 Resource Allocation attributed by GENCI.

References

[1] G. Kron, "Equivalent circuit of the field equations of Maxwell—I," *Proc. IRE*, vol. 32, no. 5, pp. 289–299, May 1944.

[2] P. B. Johns, "A symmetrical condensed node for the TLM method," *IEEE Trans. Microw. Theory Techn.*, vol. MTT-35, no. 4, pp. 370–377, Apr. 1987.

[3] J. Paul, C. Christopoulos, and D. W. P. Thomas, "Generalized material models in TLM—Part 2: Materials with anisotropic properties," *IEEE Trans. Antennas Propag.*, vol. 47, no. 10, pp. 1535–1542, Oct. 1999.

[4] J. Paul, C. Christopoulos, and D. W. P. Thomas, "Generalized material models in TLM—Part 1: Materials with frequency-dependent properties," *IEEE Trans. Antennas Propag.*, vol. 47, no. 10, pp. 1528–1534, Oct. 1999.

[5] A. L. Farhat, S. L. Maguer, P. Queffelec, and M. Ney, "TLM extension to electromagnetic field analysis of anisotropic and dispersive media: A unified field equation," *IEEE Trans. Microw. Theory Techn.*, vol. 60, no. 8, pp. 2339–2351, Aug. 2012.

[6] L. Seyyed-Kalantari, M. H. Bakr, and N. K. Nikolova, "Sensitivity analysis of ferrites with TLM," *IEEE Microw. Wireless Compon. Lett.*, vol. 27, no. 12, pp. 1044–1046, Dec. 2017.

[7] L. S. Kalantari, O. S. Ahmed, M. H. Bakr, and N. K. Nikolova, "A TLM-based wideband adjoint variable method for sensitivity analysis of non-dispersive anisotropic structures," *IEEE Trans. Antennas Propag.*, vol. 65, no. 10, pp. 5267–5278, Oct. 2017.

[8] K.-P. Hwang and A. C. Cangellaris, "Effective permittivities for second-order accurate FDTD equations at dielectric interfaces," *IEEE Microw. Wireless Compon. Lett.*, vol. 11, no. 4, pp. 158–160, Apr. 2001.

[9] A. Ijjeh, M. M. Ney, and F. Andriulli, "Behavior of time-domain volumic methods in presence of high-contrast media or irregular structured mesh interfaces," in *Proc. 9th IEEE Eur. Conf. Antennas Propag.*, Lisbon, Portugal, Apr. 2015, pp. 1–5.

[10] A. Laisné and J. Drouet, "Comparison of FIT and TLM for numerical dosimetry in HF/VHF band," in *Proc. Int. Symp. Electromagn. Compat.*, Brugge, Belgium, Sep. 2013, pp. 175–180.

[11] G. Z. Yin, Y. Q. Zhang, C. X. Yang, and M. S. Tong, "On solving volume integral equations with highly anisotropic media," in *Proc. IEEE Antennas Propag. Soc. Int. Symp. (APSURSI)*, Memphis, TN, USA, Jul. 2014, pp. 2128–2129.

[12] B. Anderson and Z. Cendes, "Three-dimensional finite element analysis of ferrite devices including spatial inhomogeneity of the permeability tensor," in *IEEE Antennas Propag. Soc. Int. Symposium. Dig.*, Baltimore, MD, USA, Jul. 1996, pp. 138–141.

[13] J. Wlodarczyk, "New multigrid interface for the TLM method," *Electron. Lett.*, vol. 32, no. 12, pp. 1111–1112, Jun. 1996.

[14] A. A. Ijjeh and M. Ney, "Local time-step TLM unstructured block meshing for electromagnetic and bio-thermal applications," *IEEE J. Multiscale Multiphys. Comput. Techn.*, vol. 2, pp. 174–182, Nov. 2017.

[15] A. Ijjeh, M. Cueille, J.-L. Dubard, and M. Ney, "Time-domain modeling and simulation of EM-fields propagation in anisotropic dispersive media with non-conformal meshing," in *Proc. 14th Eur. Conf. Antennas Propag. (EuCAP)*, Copenhagen, Denmark, Mar. 2020, pp. 1–5.

[16] A. J. Ward and J. B. Pendry, "Refraction and geometry in Maxwell's equations," *J. Modern Opt.*, vol. 43, no. 4, pp. 773–793, Apr. 1996.

[17] B. Engquist, P. Lötstedt, and O. Runborg, *Multiscale Methods in Science and Engineering*. New York, NY, USA: Springer, 2005, pp. 133–148.

[18] M. Okoniewski, E. Okoniewska, and M. A. Stuchly, "Three-dimensional subgridding algorithm for FDTD," *IEEE Trans. Antennas Propag.*, vol. 45, no. 3, pp. 422–429, Mar. 1997.

[19] R.-B. Wu and T. Itoh, "Hybrid finite-difference time-domain modeling of curved surfaces using tetrahedral edge elements," *IEEE Trans. Antennas Propag.*, vol. 45, no. 8, pp. 1302–1309, Aug. 1997.

[20] J.-P. Bérenger, "A Huygens subgridding for the FDTD method," *IEEE Trans. Antennas Propag.*, vol. 54, no. 12, pp. 3797–3804, Dec. 2006.

[21] K. Zeng and D. Jiao, "Symmetric positive semi-definite FDTD subgridding algorithms in both space and time for accurate analysis of inhomogeneous problems," *IEEE Trans. Antennas Propag.*, vol. 68, no. 4, pp. 3047–3059, Apr. 2020.

[22] Z. Ye, X. Liao, and J. Zhang, "A novel three-dimensional FDTD subgridding method for the coupling analysis of shielded cavity excited by ambient wave," *IEEE Trans. Electromagn. Compat.*, vol. 62, no. 6, pp. 2441–2449, Dec. 2020.

[23] O. Podebrad, M. Clemens, and T. Weiland, "New flexible subgridding scheme for the finite integration technique," *IEEE Trans. Magn.*, vol. 39, no. 3, pp. 1662–1665, May 2003.

[24] Q. Sun, Q. Ren, Q. Zhan, and Q. H. Liu, "3-D domain decomposition based hybrid finite-difference time-domain/finite-element time-domain method with nonconformal meshes," *IEEE Trans. Microw. Theory Techn.*, vol. 65, no. 10, pp. 3682–3688, Oct. 2017.

[25] A. A. Ijjeh, M. M. N. Ney, and F. P. Andriulli, "Stability and dispersion analysis of a TLM unified approach for dispersive anisotropic media," *IEEE Trans. Microw. Theory Techn.*, vol. 65, no. 4, pp. 1141–1149, Apr. 2017.
[26] Z. Li, "Contributions aux techniques de maillages irréguliers dans la méthode TLM: Applications Au calcul électromagnétique de structures à détails fins et interfaces non-cartésiennes," Ph.D. dissertation, Dept. MW, ENST Bretagne, Brest, France, 2005.
[27] I. Ahmed and Z. Chen, "A hybrid ADI-FDTD subgridding scheme for efficient electromagnetic computation," *Int. J. Numer. Model., Electron. Netw., Devices Fields*, vol. 17, no. 3, pp. 237–249, Apr. 2004.
[28] S. LeMaguer, A. Peden, D. Bourreau, and M. M. Ney, "Split-step TLM (SS TLM)—A new scheme for accelerating electromagnetic-field simulation," *IEEE Trans. Microw. Theory Techn.*, vol. 52, no. 4, pp. 1182–1190, Apr. 2004.
[29] G. L. Romo and T. Smy, "Derivation and numerical solution of a dispersion relation for TLM subgridded meshes," in *Proc. IEEE Antennas Propag. Soc. Int. Symp.*, Albuquerque, NM, USA, Jul.2006, pp. 1811–1814.
[30] C. Christopoulos, *The Transmission-Line Modeling (TLM) Method in Electromagnetics* (Synthesis Lectures on Computational Electromagnetics). San Rafael, CA, USA: Morgan & Claypool, 2006, pp. 65–121.
[31] P. Saguet, *Numerical Analysis in Electromagnetics: The TLM Method.* 1st ed. Hoboken, NJ, USA: Wiley, 2012, pp. 55–139.
[32] P. Russer and M. Krumpholz, "The Hilbert space formulation of the TLM method," *Int. J. Numer. Modelling: Electron. Netw., Devices Fields*, vol. 6, no. 1, pp. 29–45, Feb. 1993.
[33] M. Krumpholz and P. Russer, "A generalized method for the calculation of TLM dispersion relations," in *Proc. 23rd Eur. Microw. Conf.*, Madrid, Spain, Oct. 1993, pp. 288–290.
[34] J. S. Nielsen and W. J. R. Hoefer, "Generalized dispersion analysis and spurious modes of 2-D and 3-D TLM formulations," *IEEE Trans. Microw. Theory Techn.*, vol. 41, no. 8, pp. 1375–1384, Aug. 1993.
[35] V. Trenkic, C. Christopoulos, and T. M. Benson, "New symmetrical super-condensed node for the TLM method," *Electron. Lett.*, vol. 30, no. 4, pp. 329–330, Feb. 1994.
[36] R. Scaramuzza and A. J. Lowery, "Hybrid symmetrical condensed node for the TLM method," *Electron. Lett.*, vol. 26, no. 23, pp. 1947–1949, Nov. 1990.
[37] N. Pea and M. M. Ney, "A general formulation of a three-dimensional TLM condensed node with the modeling of electric and magnetic losses and current sources," in *Proc. 12th Annu. Rev. Progr. Appl. Comput. Electromagn.*, Monterey, CA, USA, Mar. 1996, pp. 262–269.
[38] V. Trenkic, C. Christopoulos, and T. M. Benson, "Efficient computational algorithms for TLM," in *Proc. 1st Int. Workshop TLM Modeling-Theory Applicat.*, Victoria, BC, Canada, Aug. 1995, pp. 77–80.
[39] G. Kranc, "Input-output analysis of multirate feedback systems," *IRE Trans. Autom. Control*, vol. 3, no. 1, pp. 21–28, Nov. 1957.
[40] R. F. Remis, "On the stability of the finite-difference time-domain method," *J. Comput. Phys.*, vol. 163, no. 1, pp. 249–261, Sep. 2000.
[41] A. Ijjeh, M. Ney, M. Cueille, and J.-L. Dubard, "Etude de la dispersion et des limites du schéma numérique TLM avec maillage par blocs," in *Proc. 21st JNM*, Caen, France, May 2019, pp. 462–465.
[42] J. F. Epperson, *An Introduction to Numerical Methods and Analysis*. Hoboken, NJ, USA: Wiley, 2013, pp. 90–96.

Abdelrahman A. Ijjeh received the B.S. and M.S degrees in communication engineering from Yarmouk University, Irbid, Jordan, in 2008 and 2011, respectively, and the Ph.D. degree in communication engineering from the Institut Mines-Télécom, Brest, France, in 2014.

He is currently a Research and Development Engineer with the Laboratory of Electronic, Antennas and Telecommunications (LEAT), Université Côte d'Azur, Sophia Antipolis, France. His research interests include computational electromagnetics in general complex linear media and multiscale scenarios with applications to dosimetry and hyperthermia.

Marylène Cueille (Member, IEEE) received the Ph.D. degree in electronic of high frequency from the University of Limoges, Limoges, France, 2007.

Since 2009, she has been an Assistant Professor with the Université Côte d'Azur (UCA), Sophia Antipolis, France. She is doing her research at the Laboratory of Electronic, Antennas and Telecommunications (LEAT), French National Research Council (CNRS)-UMR 7248, UCA. Her research areas of interest include numerical multiscale and multiphysic antennas simulations based on the transmission-line matrix (TLM) method, in particular, electromagnetism and thermal phenomena for bioelectromagnetism and physical applications.

Jean-Lou Dubard (Member, IEEE) received the Ph.D. degree in electrical engineering from the University of Nice Sophia Antipolis, Nice, France, in 1992.

Since 1993, he has been a Researcher with the Laboratory of Electronics, Antennas and Telecommunications (LEAT), French National Research Council (CNRS), Université Côte d'Azur, Sophia Antipolis, France. He has been a Professor with the Université Côte d'Azur since 2007. His research focuses on numerical modeling techniques for multiscale and multiphysics problems dedicated to antennas' interactions with surrounding media from very low frequency (VLF) to microwave frequencies.

Michel M. Ney (Life Fellow, IEEE) received the Engineering Diploma degree from the Swiss Federal Institute of Technology (EPFL), Lausanne, Switzerland, in 1976, the M.Sc. degree from the University of Manitoba, Winnipeg, MB, Canada, in 1978, and the Ph.D. degree from the University of Ottawa, Ottawa, ON, Canada, in 1983.

He started his academic career as an Assistant Professor at the University of Ottawa. He was a Research Engineer with the Laboratory of Electromagnetism and Acoustics (LEMA), EPFL, for two years. He spent his sabbatical year at the Swiss Federal Institute of Technology, Zürich, Switzerland, as a Guest Professor, in 1989. He became a Full Professor in June 1993 and shortly after joined the Mine-Telecom Institute ("IMT Atlantique," previously "Telecom Bretagne"), a graduate engineering school in Brest, France. He was the Head of the Laboratory for Electronics and Communication Systems (LEST), French National Research Council (CNRS), Sophia Antipolis, France, from 1998 to 2007, and the President of the French URSI Commission B "Field and Waves" from 2007 to 2009. He has been an Emeritus with the IMT Atlantique since 2018. His research interests include computational electromagnetics in the time domain with applications mainly focused on the antenna, dosimetry, and multiphysics problems.

Prof. Ney has been a member of the Editorial Board of the *International Journal of Numerical Modelling: Electronic Networks, Devices and Fields* (John Wiley) since 1987. He was a member of the Advisory Board of the *Annals of Telecommunications* (Springer) until 2016 and a member of the Permanent Scientific Committee of the International Colloquium and Exhibitions on Electromagnetic Compatibility (in French) from 1993 to 2018.